Sweet Pluronic poly(propylene oxide)-*b*-oligosaccharide block copolymer systems: Toward sub-4 nm thin-film nanopattern resolution[1]

Muhammad Mumtaz[a], Yasuko Takagi[b], Hiroaki Mamiya[c], Kenji Tajima[d], Cécile Bouilhac[e], Takuya Isono[d], Toshifumi Satoh[d*], and Redouane Borsali[a*]

[a]*Univ. Grenoble Alpes, CNRS, CERMAV, 38000 France.*

[b]*Graduate School of Chemical Sciences and Engineering, Hokkaido University, Sapporo 060 8628, Japan*

[c]*National Institute for Materials Science, Tsukuba 305-0047, Japan.*

[d]*Faculty of Engineering, Hokkaido University, Sapporo 060 8628, Japan*

[e]*Univ. Montpellier, CNRS, ENSCM, ICGM, Montpellier, France*

[*]*Corresponding authors: borsali@cermav.cnrs.fr; satoh@eng.hokudai.ac.jp*

[1] Abbreviations: block copolymer(s) (BCP(s)); poly(propylene oxide) (PPO); extreme ultraviolet lithography (EUVL); directed self-assembly (DSA); poly(ethylene oxide) (PEO); ω-tosyl poly(propylene glycol) (PPO-Ts); α,ω-ditosyl poly(propylene glycol) (Ts-PPO-Ts); maltoheptaose (MH); maltotriose (MT); maltose (Mal); size-exclusion chromatography (SEC); synchrotron small-angle X-ray scattering (SAXS); hexagonally close-packed cylindrical (HEX); body-centered cubic (BCC); lamellar (LAM); order-to-disorder transition (ODT); atomic force microscopy (AFM); grazing-incidence small-angle X-ray scattering (GISAXS); high-temperature solvent vapor annealing (HTSVA); trimethylamine (TEA); tetrahydrofuran (THF); N,N-dimethylformamide (DMF); Cu/CuO nanopowder (CuNP); European Synchrotron Radiation Facility (ESRF)

Abstract

Block copolymers (BCPs) with a high Flory−Huggins interaction parameter (χ) are promising alternatives to conventional nanopatterning materials for future nanolithography and nanotechnology applications. Herein, we described AB- and ABA-type BCPs comprising oligosaccharides (maltoheptaose, maltotriose, and maltose as the A block) and poly(propylene oxide) (PPO, as the B block) as new high-χ BCP systems, which can be termed "Sweet Pluronics". The BCPs were successfully synthesized by click reaction between azido-functionalized PPO and propargyl-functionalized maltooligosaccharides. These BCPs undergo microphase separation in bulk state to provide various nanopatterns, i.e., sub-4 nm nanofeatures (cylinders, lamellae, and spheres) with domain spacing as low as 6.2 nm, depending on their composition and the applied annealing conditions. The thin film of these BCPs fabricated on a silicon substrate also showed various microphase-separated structures. When the BCP thin films were subjected to high-temperature solvent vapor annealing using a μ-wave oven as the heating source, their morphologies changed from parallel lamellar to cylindrical because of the preferential swelling of PPO. Overall, these results confirmed that the present "Sweet Pluronics" system is promising high-χ materials for sub-4 nm nanopatterning applications.

Keywords: block copolymer, self-assembly, microphase separation, oligosaccharide, thin film

Introduction

Due to their ability to undergo microphase separation into various nanofeatures including lamellae, hexagonally packed cylinders, double gyroids, and body-centered cubic (BCC) spheres, AB- and ABA-type block copolymers (BCPs) have attracted significant attention in the semiconductor and nanofabrication industries. These ordered structures have domain sizes ranging from 2 to 100 nm and have been used as templates to fabricate quantum dots, nanowires, magnetic storage media, nanopores, and silicon capacitors [1–6]. Integrated circuits with faster processing speeds, higher storage capacity, significant size reduction, and lower energy requirements have characterized the microelectronics industry. However, the current 193-nm patterning technology is approaching its resolution limit, and although extreme ultraviolet lithography (EUVL) is being developed as the next-generation patterning technology for the 7 nm node, due to its high cost and limited throughput, its application for semiconductor manufacturing still remains a challenging task [7–11]. Directed self-assembly (DSA) of block polymer systems represents an attractive "bottom-up" alternative to EUVL and multiple patterning techniques as via this method, the block polymer systems can self-assemble into nanoscopic periodic patterns over large areas [12–21]. The phase behavior of the AB- and ABA-type BCPs depends on the volume fraction of the A block (f_A), degree of polymerization (N), Flory−Huggins interaction parameter (χ), and molecular architecture. The distance between microphase-separated domains, called domain spacing (d), scales as $d \sim N^{2/3} \chi^{1/6}$ in the strong segregation limit [22–24]; therefore, developing BCPs with a high χ and lower total N is a strategy used by several researchers for obtaining a small feature size in the BCP self-assembly [25–35].

In our previous investigations, we have found that oligosaccharides are useful building blocks for designing BCPs capable of self-assembling into microphase-separated structures of sub-10 nm domain size [36–40]. In these systems, the strong hydrophilicity imparted by the presence

of multiple hydroxyl groups results in oligosaccharide-containing amphiphilic BCPs with high χ values, and the rigidity of the carbohydrate backbone further enhances the incompatibility of the hydrophilic block with the hydrophobic block. Additionally, Hillmyer's and Sita's groups have recently reported sugar-based amphiphiles and sugar-based BCPs, respectively, which can self-assemble into ultra-small nanodomains [41,42]. Furthermore, we have reported that the thin films of oligosaccharide-based BCPs can self-assemble into longer-range ordered, standing nanodomains in a few seconds using μ-wave energy as a heating source in both the presence and absence of annealing solvent vapors [43,44]. Therefore, further expansion of the oligosaccharide-based BCP system is of fundamental interest for future nanotechnology applications.

Herein, we report a novel family of oligosaccharide-based BCPs, consisting of maltooligosaccharide and poly(propylene oxide) (PPO), capable of forming ultra-small microphase-separated structures. PPO is well-known as the hydrophobic part of Pluronics, which are amphiphilic BCPs consisting of poly(ethylene oxide) (PEO) and PPO [45]. Pluronics are used in various applications such as in detergents, emulsifiers, gelation agents, nanotemplates for porous material preparation, and drug nanocarriers, where the self-assembly behaviors driven by the amphiphilic nature of Pluronics play an important role [45–48]. However, most of the neat Pluronics do not undergo microphase separation due to their small χ and N values [49,50]; this has limited their nanotechnology applications in the bulk and thin film states. Thus, our idea is to replace the PEO block by an oligosaccharide to achieve Pluronics with high χ values; such BCPs can be termed as "Sweet Pluronics". Specifically, herein, we synthesized an AB-type diblock copolymer (PPO_{2k}-*b*-MT) and ABA-type triblock copolymers (Mal-*b*-PPO_{2k}-*b*-Mal, MT-*b*-$PPO_{2k\ or\ 4k}$-*b*-MT, and MH-*b*-$PPO_{2k\ or\ 4k}$-*b*-MH), in which maltose (Mal), maltotriose (MT), and maltoheptaose (MH) were used as the oligosaccharide block, by a click reaction between azido-functionalized PPOs and propargyl-

functionalized maltooligosaccharides. These BCPs were examined in both the bulk and thin film states by small-angle X-ray scattering and imaging techniques, revealing the formation of lamellar (LAM), cylindrical, and spherical nanostructures (sub-4 nm nanofeatures) with *d* as low as 6.2 nm. Note that Akiyoshi et al. reported similar BCPs for application in vesicle formation in aqueous media during the course of our current study [51]. Nevertheless, this is the first study to demonstrate the microphase separation of an oligosaccharide/PPO BCP system.

Results and discussion

Synthesis of BCPs. To prepare PPO-based BCPs, initially, commercially available poly(propylene glycol) monobutyl ether and poly(propylene glycols) with different molecular weights were reacted with *p*-toluenesulfonyl chloride in the presence of trimethylamine (TEA) to obtain *ω*-tosyl poly(propylene glycol) (PPO-Ts) and *α*,*ω*-ditosyl poly(propylene glycol) (Ts-PPO-Ts), respectively; subsequently, PPO-Ts and Ts-PPO-Ts were treated with NaN_3 in *N*,*N*-dimethylformamide (DMF) at 60 °C overnight to synthesize azido-functionalized PPOs (PPO-N_3 and N_3-PPO-N_3, respectively) in good yields (Scheme 1).

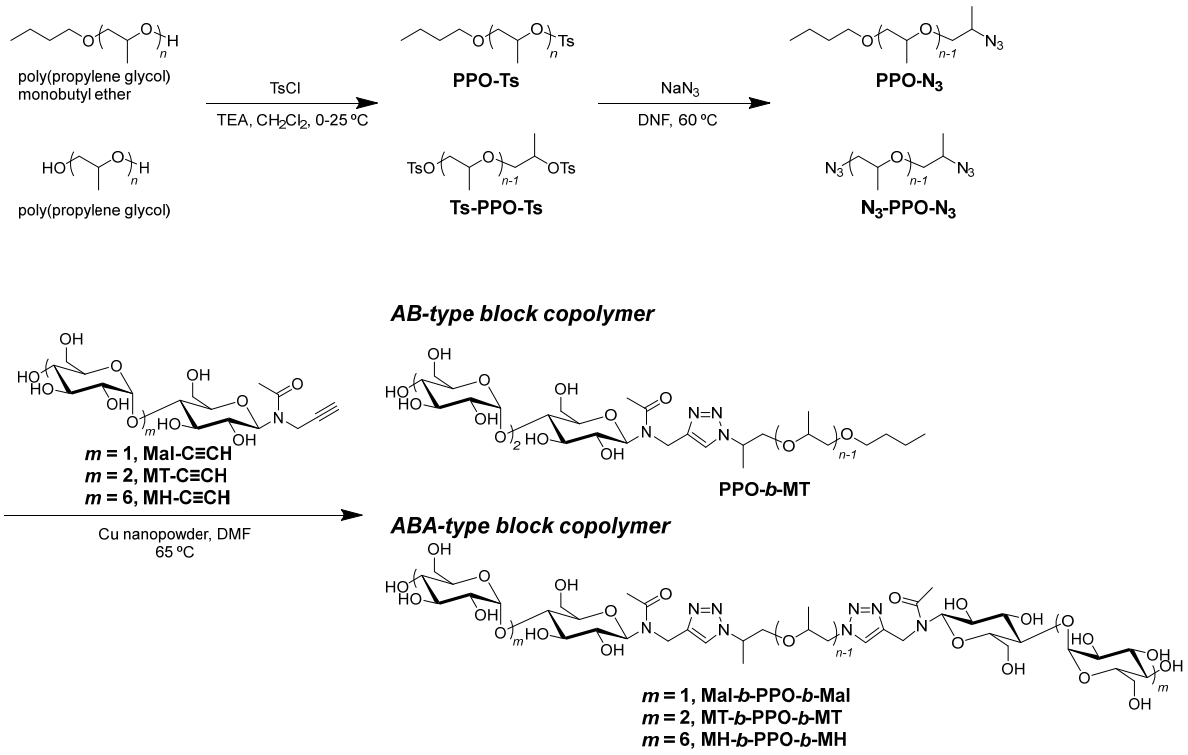

Scheme 1. Synthesis of AB- and ABA-type block copolymers consisting of oligosaccharides (maltoheptaose (MH), maltotriose (MT), or maltose (Mal)) as the A block and poly(propylene oxide) (PPO) as the B block.

The ^{1}H NMR spectra of a representative azido-functionalized PPO, N_3-PPO_{2k}-N_3, and its precursors are shown in Figure S1. The disappearance of the signals positioned at 3.90 ppm and

~3.19 ppm corresponding to –C***H***(CH_3)-OH and –C***H***$_2$-OH of poly(propylene glycol), respectively, and appearance of signals at 7.30–7.80 ppm due to the tosyl group confirmed the synthesis of Ts-PPO-Ts. Finally, the disappearance of the signals corresponding to the tosyl group after the treatment of Ts-PPO-Ts with NaN_3 indicated the formation of N_3-PPO-N_3. The appearance of an absorption band at ~2100 cm^{-1} due to the azido group in the FTIR spectrum (Figure S2) further confirmed the azido-end functionalization of PPO.

The BCPs were prepared by the click reaction of azido end-functionalized PPOs with propargyl end-functionalized oligosaccharides (Mal-C≡CH, MT-C≡CH, and MH-C≡CH) in DMF in the presence of Cu/CuO nanopowder (CuNP) as a catalyst. The complete disappearance of the abovementioned absorption band at ~2100 cm^{-1} confirmed the quantitative conversion of the azido end-functionalized PPOs into the corresponding BCPs (Figure S2).

The BCPs were further characterized by ^{1}H NMR spectroscopy and size-exclusion chromatography (SEC). The ^{1}H NMR spectrum of MT-*b*-PPO_{2k}-*b*-MT is shown in Figure 1. The appearance of signals at 8.07–8.26 ppm, 6.10–3.80 ppm, and 1.1 ppm due to the triazole ring proton, oligosaccharides, and methyl group of the PPO backbone, respectively, confirmed the formation of the BCPs. The molecular weight and composition of the BCPs could be determined by the relative integration of the signals located at 1.1 ppm due to the methyl group of the PPO backbone and at 5.15 ppm due to the C1 protons of the oligosaccharide units. The SEC results revealed a clear shift of the elution peak toward the higher-molecular-weight region upon the click reaction; this is good evidence for the successful formation of the desired BCPs via the click reaction (Figure 2).

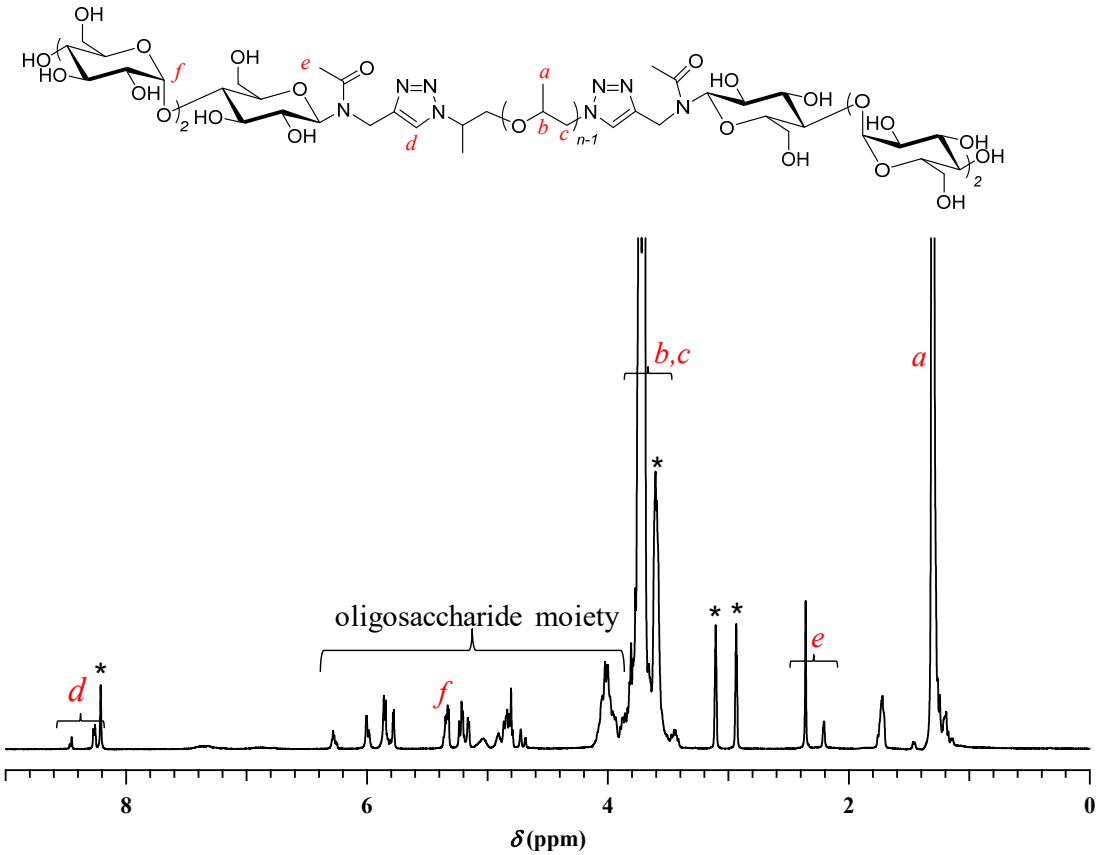

Figure 1. ^{1}H NMR spectrum of MT-*b*-PPO$_{2k}$-*b*-MT (400 MHz, DMF-d_7, 25 °C). The asterisks represent the peaks of the contaminated DMF and H_2O in the D-solvent.

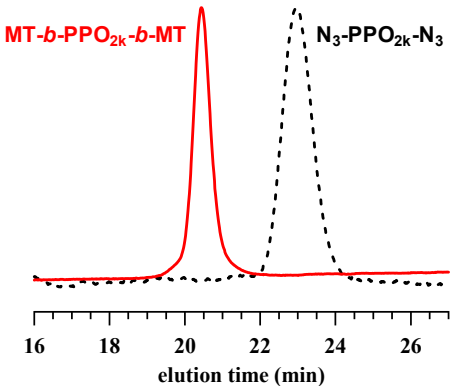

Figure 2. SEC profiles of MT-*b*-PPO$_{2k}$-*b*-MT (red) and the corresponding azido end-functionalized N_3-PPO$_{2k}$-N_3 (black) in DMF (containing 0.01 M LiCl) at 40 °C.

The molecular characteristics of the BCPs with different molecular weights and compositions are presented in Table 1. It is apparent from the data shown in Table 1 that well-defined BCPs with expected molecular weights were prepared except for MH-*b*-PPO_{2k}-*b*-MH, wherein the calculated molecular weight of MH was lower than the expected molecular weight because of the presence of some diblock copolymers in this sample.

Table 1. Characteristics of the AB- and ABA-type block copolymers.

Sample	M_n of PPO[a] (g mol^{-1})	$M_{n,Total}$[a] (g mol^{-1})	$M_{n,SEC}$[b] (g mol^{-1})	$Đ$[b]	$f_{oligosaccharide}$[c]
PPO_{2k}-b-MT	2160	2740	4430	1.14	0.13
MT-*b*-PPO_{4k}-*b*-MT	4380	5550	9380	1.24	0.13
MT-*b*-PPO_{2k}-*b*-MT	2000	3160	12900	1.08	0.25
MH-*b*-PPO_{2k}-*b*-MH	2000	4025	20250	1.14	0.43
MH-*b*-PPO_{4k}-*b*-MH	4000	6420	27800	1.15	0.31
Mal-*b*-PPO_{2k}-*b*-Mal	2000	2680	10600	1.12	0.18

[a] Determined by ^{1}H NMR. [b] Determined by SEC in DMF (containing 0.01 M LiCl) based on polystyrene calibration. [c] Oligosaccharide volume fraction ($f_{oligosaccharide}$) was calculated based on the molecular weight and density value of each block.

Morphologies in the bulk. The diblock and triblock copolymers composed of PPO and oligosaccharide blocks are expected to exhibit microphase separation due to the strong immiscibility of these two blocks. To obtain information regarding the nanostructures present in the bulk state, small-angle X-ray scattering (SAXS) experiments were performed at ambient temperature on the bulk samples before and after thermal annealing (at 80, 130, and 180 °C for 30 min), as summarized in Figures 3–5. The clearly observable primary scattering peaks in all the SAXS profiles indicated that the PPO and oligosaccharide blocks were apparently phase-separated.

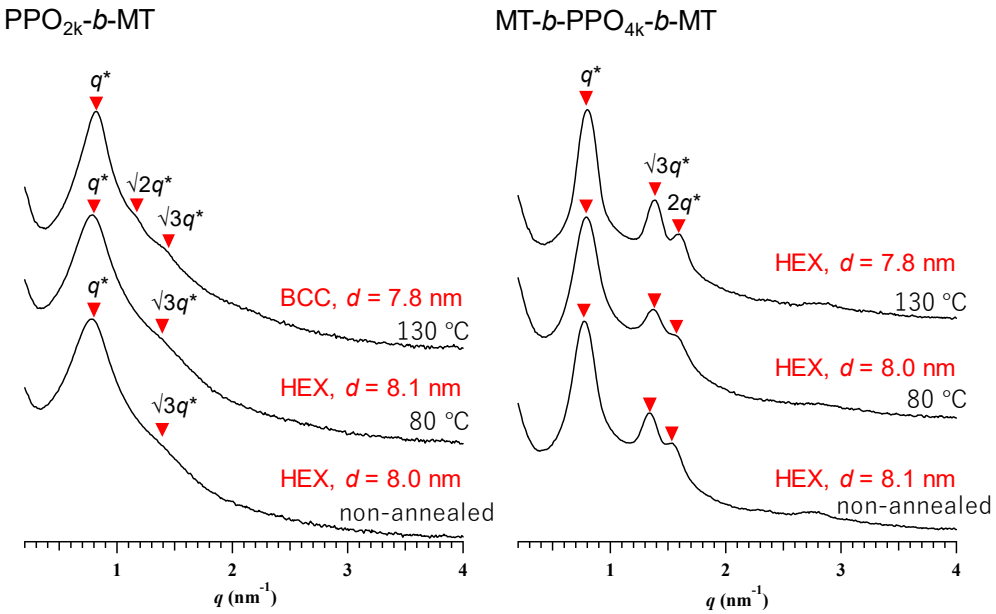

Figure 3. SAXS profiles of the bulk PPO_{2k}-*b*-MT and MT-*b*-PPO_{4k}-*b*-MT samples before and after thermal annealing at 80 and 130 °C for 30 min. All SAXS experiments were performed at room temperature.

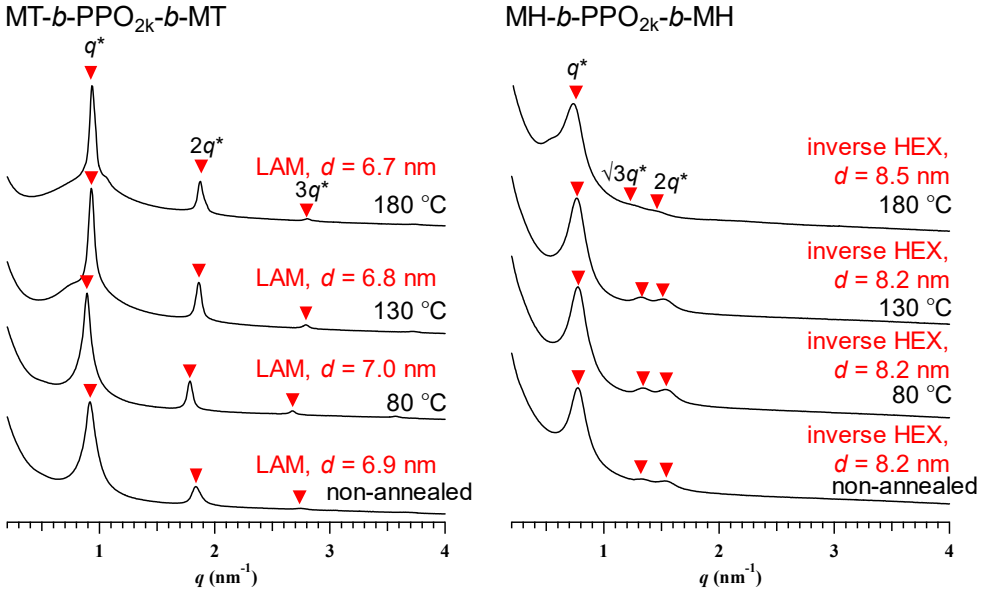

Figure 4. SAXS profiles of the bulk MT-*b*-PPO_{2k}-*b*-MT and MH-*b*-PPO_{2k}-*b*-MH samples before and after thermal annealing at 80, 130, and 180 °C for 30 min. All SAXS experiments were performed at room temperature.

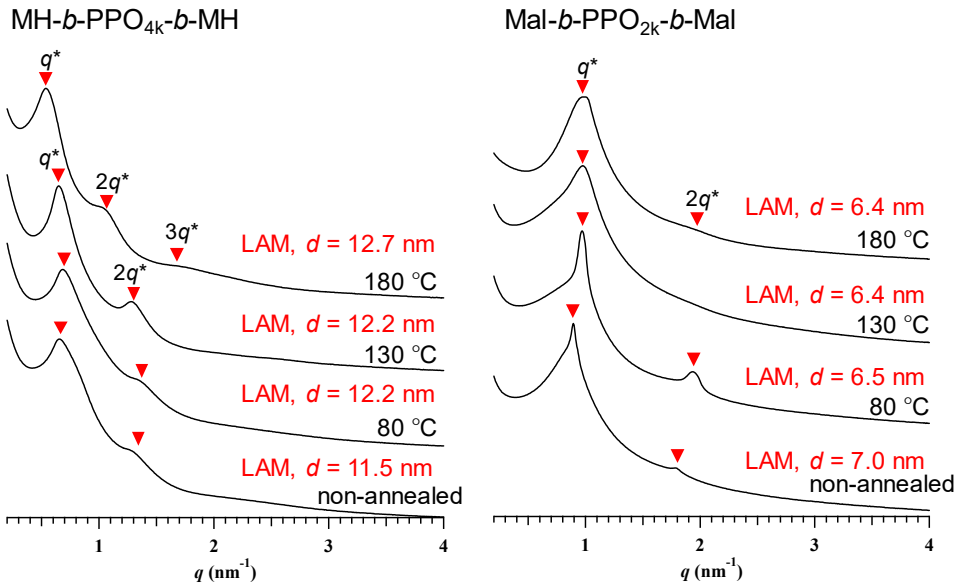

Figure 5. SAXS profiles for the bulk MH-*b*-PPO$_{4k}$-*b*-MH and Mal-*b*-PPO$_{4k}$-*b*-Mal samples before and after thermal annealing at 80, 130, and 180 °C for 30 min. All SAXS experiments were performed at room temperature.

The BCPs provided different sets of scattering patterns depending on their composition. As shown in Figure 3, prior to thermal annealing, PPO$_{2k}$-*b*-MT exhibited a primary scattering peak at $q^* = 0.7850$ nm^{-1} along with a weak secondary scattering peak at $\sqrt{3}q^*$, corresponding to a hexagonally close-packed cylindrical (HEX) phase. As the volume fraction of the PPO block is significantly greater than that of the MT block, the cylindrical domain and the matrix should be assigned to MT and PPO, respectively. The *d* value for the HEX phase was determined to be 8.0 nm using the relationship $d = 2\pi/q^*$. When PPO$_{2k}$-*b*-MT was annealed at 80 °C, a scattering pattern identical to that of non-annealed PPO$_{2k}$-*b*-MT was observed, indicating that no change in morphology and *d* occurred after annealing. Contrarily, after thermal annealing at 130 °C, a change in the scattering pattern was observed. The appearance of higher-order scattering peaks at $\sqrt{2}q^*$ and $\sqrt{3}q^*$ suggested the formation of a BCC spherical structure with a *d* of 7.8 nm. This kind of order-to-order transition has been found in the BCPs exhibiting an upper critical ordering transition, where χ decreases with the increasing temperature [52–54].

Interestingly, MT-*b*-PPO$_{4k}$-*b*-MT, having the same $f_{oligosaccharide}$ as PPO$_{2k}$-*b*-MT, exhibited a SAXS profile with sharp and higher-order scattering peaks, indicating a well-defined longer-range-ordered HEX morphology (Figure 1). Herein, no difference in the scattering pattern and peak intensity was observed in the SAXS profiles of MT-*b*-PPO$_{4k}$-*b*-MT before and after annealing; this suggests that the morphologies formed by MT-*b*-PPO$_{4k}$-*b*-MT are more stable than those formed by PPO$_{2k}$-*b*-MT. This could be due to the ABA-type architecture of MT-*b*-PPO$_{4k}$-*b*-MT, which can cause crosslinking between the cylindrical domains in this particular case, restricting the chain mobility and eventually morphological transition. The *d* calculated from the first-order peak prior to annealing was found to be 8.1 nm, which slightly decreased to 7.8 nm upon annealing (at 130 °C) due to the decrease in χ with the increasing temperature.

Herein, conventional PPO-*b*-PEO and PEO-*b*-PPO-*b*-PEO, having the total molecular weight and hydrophilic/hydrophobic ratio comparable to those of PPO$_{2k}$-*b*-MT and MT-*b*-PPO$_{4k}$-*b*-MT, respectively, did not undergo microphase separation. The SAXS profiles of PPO-*b*-PEO and PEO-*b*-PPO-*b*-PEO obtained at room temperature showed featureless scattering and a broad peak (Figure S3), respectively, suggesting that the segregation strength between the PPO and PEO blocks is significantly less than the critical values ($\chi N < 10.5$). That is, replacing the hydrophilic PEO block by an oligosaccharide substantially enhanced the incompatibility of the hydrophilic block with the PPO block; this made the formation of the microphase-separated structures possible despite the low *N* of the oligosaccharide-containing PPOs.

When the $f_{oligosaccharide}$ was doubled (MT-*b*-PPO$_{2k}$-*b*-MT; $f_{oligosaccharide} = 0.25$) by decreasing the molecular weight of the central PPO block, the scattering peaks appeared at q^*, $2q^*$, and $3q^*$, indicating the LAM morphology (Figure 4). The presence of sharp and higher-order peaks implies the formation of well-defined longer-range ordered nanostructures. The scattering peaks became significantly sharper upon annealing MT-*b*-PPO$_{2k}$-*b*-MT, thereby suggesting that

the thermal treatment facilitated the development of microphase-separated structures, leading to the formation of nanostructures with higher degrees of ordering. The *d* is approximately 7 nm, which makes MT-*b*-PPO$_{2k}$-*b*-MT a promising material for the production of sub-4 nm patterning for future nanolithography applications.

Interestingly, when the $f_{oligosaccharide}$ was further increased by introducing MH as side blocks (MH-*b*-PPO$_{2k}$-*b*-MH; $f_{oligosaccharide}$ = 0.43), scattering peaks appeared at q^*, $\sqrt{3}q^*$, and $2q^*$ in the SAXS profiles of both the annealed and non-annealed samples, suggesting the formation of the HEX morphology. Considering the abovementioned results, it can be concluded that the formation of inverse cylinders, i.e., PPO cylinders, occurred in the oligosaccharide matrix in this case. The *d* calculated from the first-order peaks was 8.2–8.5 nm.

When the molecular weight of the central block was increased to 4k with MH as the side blocks (MH-*b*-PPO$_{4k}$-*b*-MH; $f_{oligosaccharide}$ = 0.31), the BCP microphase-separated to a LAM morphology with a *d* of 11.5–12.7 nm, as suggested by its SAXS profile (Figure 5).

Finally, to further reduce the *d*, the side blocks were replaced with Mal, having only two sugar units (Mal-*b*-PPO$_{2k}$-*b*-Mal; $f_{oligosaccharide}$ = 0.18). The non-annealed sample and the sample annealed at 80 °C exhibited scattering peaks corresponding to the LAM morphology (Figure 5). However, an increase in the annealing temperature above 80 °C led to broadening of the first-order peak and disappearance of the secondary peak, indicating an order-to-disorder transition (ODT). This phenomenon could be explained by the fact that Mal has a lower molecular weight and lower glass transition temperature (93 °C) than MT (134 °C) [55] and MH (161 °C) [56], leading to less hydrogen bonding among sugar units and higher chain mobility. These factors reduced χ, which eventually caused an ODT in Mal-*b*-PPO$_{2k}$-*b*-Mal at lower annealing temperatures than that in the case of the BCPs with MT and MH as the side blocks. The *d* calculated from the first-order peak was 6.4–7.0 nm, indicating that *d* decreased upon

decreasing the molecular weight of the oligosaccharide block. These SAXS results confirmed that the present triblock copolymer system is particularly promising for sub-4 nm nanopatterning applications.

Morphologies in thin films. To investigate the thin film morphologies, which are very important for the potential application of oligosaccharide-based BCPs in nanotechnology such as in nanolithography, atomic force microscopy (AFM) and grazing-incidence small-angle X-ray scattering (GISAXS) were employed. GISAXS is a particularly important technique for studying thin film morphologies because it provides not only an idea about the surface morphologies but also information about the orientation and nature of microdomains inside the thin film up to a certain depth; contrarily, AFM only reveals the surface texture of the thin film. The copolymer thin films were obtained by spin coating a 2 wt.% copolymer solution in ethanol at 2000 rpm on smooth silicon wafers followed by thermal treatment in a preheated oven under vacuum and/or high-temperature solvent vapor annealing (HTSVA) using μ-wave as the heating source. The thickness of these films was in the 40–60 nm range, as determined by reflectometry. The AFM phase images of the as-cast and thermally annealed PPO_{2k}-*b*-MT films and their corresponding GISAXS profiles are shown in Figure 6. The AFM phase image of the as-cast thin films demonstrates a fingerprint-like pattern corresponding to the horizontally orientated HEX morphologies. The apparent order of the thin film morphologies improved with the increasing annealing temperature because of the increase in chain mobility (Figures 6a–c). The periodicity of the as-cast film, as measured by the fast Fourier transform of the AFM phase image (d_{AFM}), was ca. 8 nm, which slightly decreased with the increasing temperature probably due to better packing in the annealed samples and is in agreement with the SAXS results. To further study the microphase-separated structures of PPO_{2k}-*b*-MT deep inside the thin-film samples employed for the AFM observations, the GISAXS experiments were performed. As shown in Figure 6d, the as-cast PPO_{2k}-*b*-MT films exhibited horizontally oriented HEX

morphologies. The appearance of sharper and second-order peaks in the GISAXS profile of the sample thermally annealed at 80 °C revealed the presence of a longer-range ordered morphology (Figure 6e). The formation of a parallel LAM morphology along with the horizontally oriented HEX morphology was indicated by the GISAXS profile of the sample thermally annealed at 130 °C. The parallel LAM formation in this highly asymmetric BCP could be due to the presence of a local gradient in composition produced by the movement of some PPO molecules toward the surface to reduce the interfacial energy difference at the air/polymer interface during annealing close to the glass transition temperature of MT (134 °C) [55]. The increase in the chain mobility and decrease in χ at high temperatures probably triggered this phenomenon.

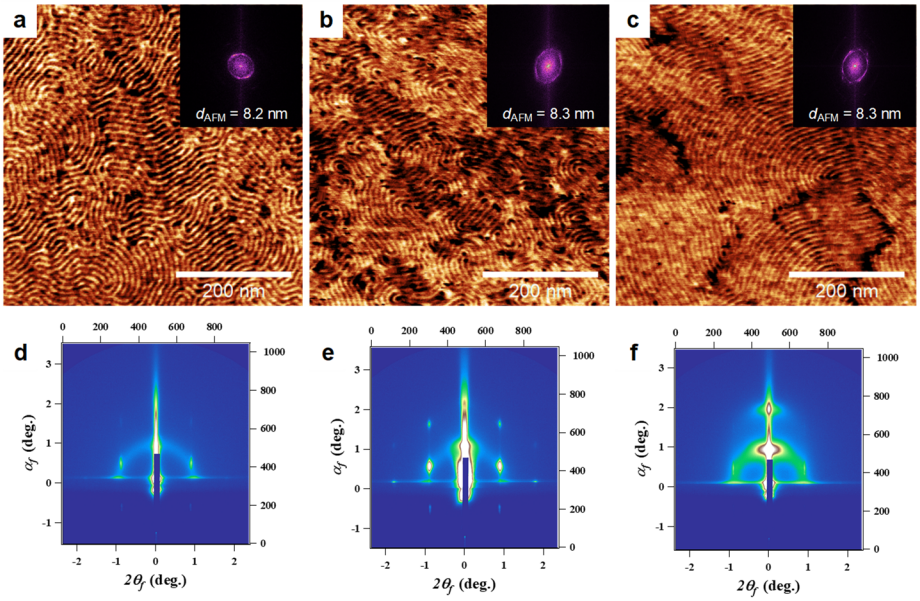

Figure 6. AFM phase images of PPO_{2k}-*b*-MT before and after thermal annealing at different temperatures: (a) as-cast sample and samples annealed at (b) 80 and (c) 130 °C for 30 min; (d), (e), and (f) are their corresponding synchrotron GISAXS profiles. The insets in the AFM images show the corresponding FFT patterns, from which the d_{AFM} was estimated. The thin films were prepared by spin coating a 2 wt% copolymer solution in ethanol onto a silicon substrate.

Similar results were obtained for MT-*b*-PPO_{4k}-*b*-MT having the same composition as PPO_{2k}-*b*-MT (Figure 7); however, less intense GISAXS scattering peaks were observed in this case.

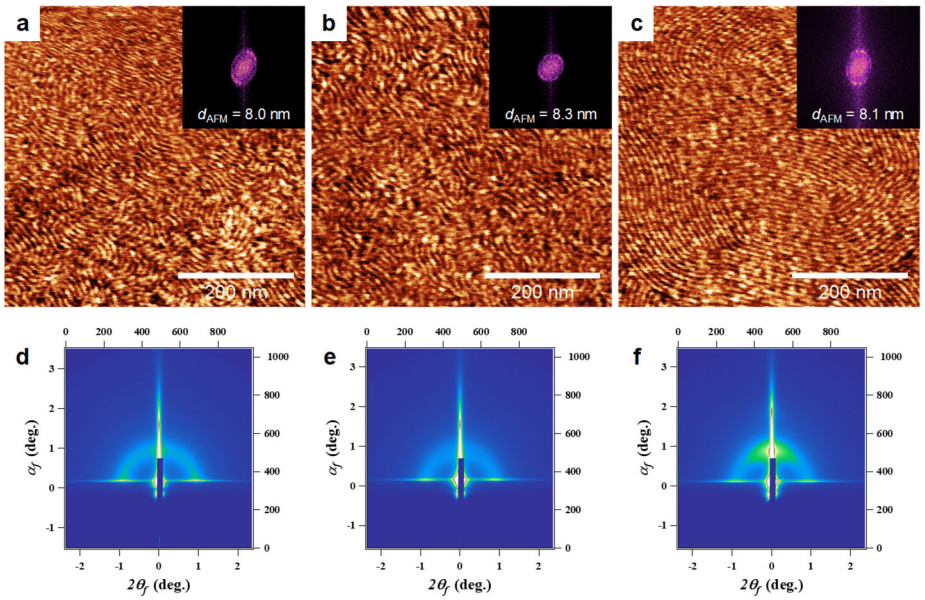

Figure 7. AFM phase images of MT-*b*-PPO$_{4k}$-*b*-MT before and after thermal annealing at different temperatures: (a) as-cast sample and samples annealed at (b) 80 and (c) 130 °C for 30 min; (d), (e), and (f) are their corresponding synchrotron GISAXS profiles. The insets in the AFM images show the corresponding FFT patterns, from which the d_{AFM} was estimated. The thin films were prepared by spin coating a 2 wt% copolymer solution in ethanol onto a silicon substrate.

For the as-cast and thermally annealed thin films of MT-*b*-PPO$_{2k}$-*b*-MT, which has a double $f_{oligosaccharide}$ as compared to that of MT-*b*-PPO$_{4k}$-*b*-MT, no nanostructure was observed in the AFM images (Figures 8a and b, respectively). When these films were examined using GISAXS, scattering spots were observed along the q_z direction in both cases (Figures 8d and e), clearly indicating the formation of the parallel LAM morphology along with the bulk morphology as observed in the case of the abovementioned SAXS analysis. The parallel LAM orientation is common in low-molecular-weight high-χ BCPs, where the surface energy difference between the BCP (with highly incompatible blocks) and the substrate as well as air at their interfaces is very high. As the surface energies of PPO and oligosaccharides are not identical, one block will interact more with the substrate than the other; this results in the parallel LAM morphology.

HTSVA has the advantages of both the solvent vapor and thermal annealing routes and causes microphase segregation within seconds [43,44]. During this ultrafast self-assembly, the BCPs do not have enough time to adjust their conformations, and the perpendicular orientation is kinetically favored. To test this hypothesis, MT-*b*-PPO_{2k}-*b*-MT was annealed at 100 °C using a μ-wave oven as the heating source in the presence of a tetrahydrofuran (THF)/H_2O (75/25, w/w) mixture for 5 s. Interestingly, the microphase-separated structure was clearly observed in the AFM phase image (Figure 8c), and based on the SAXS results, we considered it to be a vertical LAM structure. However, the GISAXS profile of this sample showed the formation of the horizontally orientated HEX structure. In fact, the presence of solvent vapors dominated by THF causes preferential swelling of the PPO block, leading to the transition from the LAM to the HEX morphology.

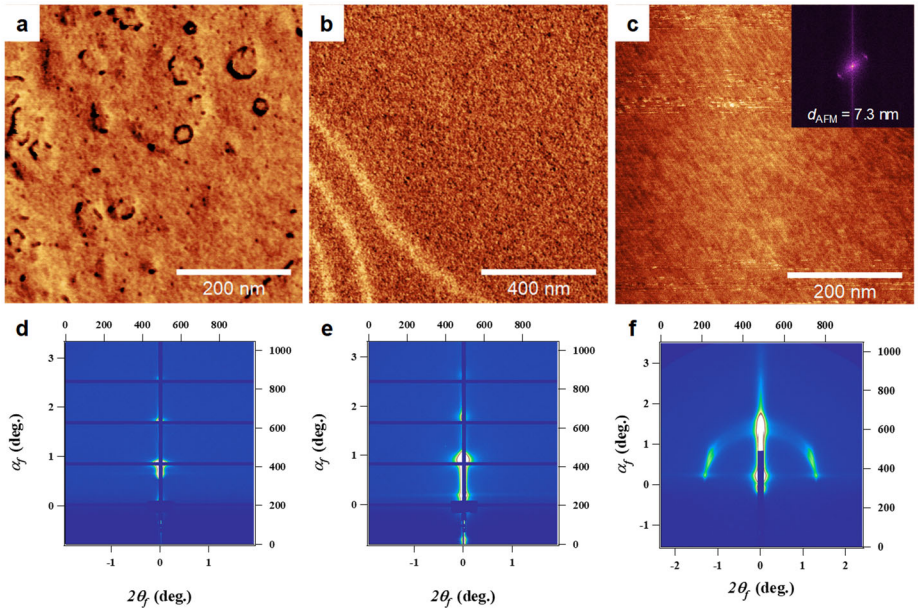

Figure 8. AFM phase images of the MT-*b*-PPO_{2k}-*b*-MT thin films prepared using different annealing techniques: (a) as-cast thin film and thin films obtained by (b) thermal annealing at 130 °C for 30 min and (c) μ-wave annealing in the presence of THF/H_2O (75:25, w/w) at 100 °C for 5 s. The inset in the AFM image (c) shows the corresponding FFT, from which the d_{AFM} was estimated. (d), (e), and (f) are the corresponding synchrotron GISAXS profiles. The thin films were prepared by spin coating a 2 wt% copolymer solution in ethanol+3 drops of DMF onto a silicon substrate.

When the $f_{\text{oligosaccharide}}$ was further increased by introducing MH instead of MT (MH-*b*-PPO_{2k}-*b*-MH), the HEX morphologies were obtained in both the non-annealed and annealed thin film samples (Figure 9). Both the as-cast and thermally annealed (130 °C, 30 min) thin films showed poorly ordered horizontally oriented HEX morphologies, as indicated in their AFM phase images (Figures 9a and b) and the GISAXS profiles (Figures 9d and e), respectively. Excitingly, vertical PPO cylinders embedded inside the MH matrix with a *d* of approximately 8 nm were clearly observed in the AFM phase image of the MH-*b*-PPO_{2k}-*b*-MH sample (Figure 9c) prepared using HTSVA. The FFT pattern shows a hexagonal packing of these cylinders. Nevertheless, when this sample was analyzed by GISAXS, the scattering pattern indicated the presence of the horizontally orientated HEX morphology, which could have originated due to different interfacial energies at the substrate/copolymer and copolymer/air interfaces. The vertical cylinders were formed on the outer surface layer, while the horizontal cylinders existed in the inner layers of the thin film.

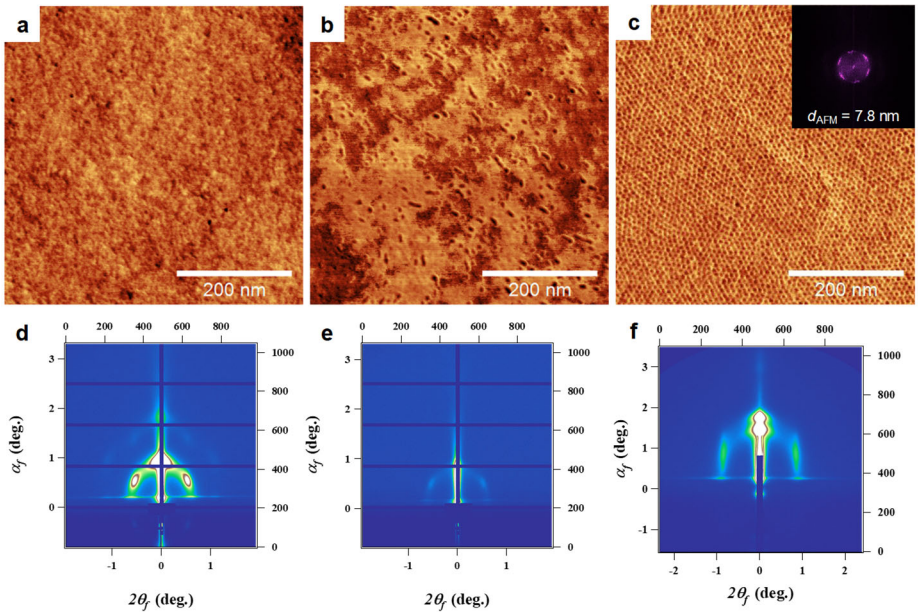

Figure 9. AFM phase images of the MH-*b*-PPO$_{2k}$-*b*-MH thin films prepared using different annealing techniques: (a) as-cast thin film and thin films obtained by (b) thermal annealing at 130 °C for 30 min and (c) μ-wave annealing in the presence of THF/H_2O (75:25, w/w) at 100 °C for 10 s. The inset in the AFM image (c) shows the corresponding FFT pattern, from which the d_{AFM} was estimated. (d), (e), and (f) are their corresponding synchrotron GISAXS profiles. The thin films were prepared by spin coating a 2 wt% copolymer solution in ethanol+3 drops of DMF onto a silicon substrate.

Similar to MT-*b*-PPO$_{2k}$-*b*-MT, MH-*b*-PPO$_{4k}$-*b*-MH and Mal-*b*-PPO$_{2k}$-*b*-Mal also showed a transition from the LAM morphology in the bulk state to the HEX morphology in the thin film state upon HTSVA using μ-wave energy at different temperatures and annealing times (Figures 10 and S4). As shown in the AFM phase images, all the MH-*b*-PPO$_{4k}$-*b*-MH samples exhibited a similar order, i.e., horizontally orientated HEX, in their morphologies independent of the annealing temperature and time; this was further confirmed by their GISAXS profiles (Figures 10e–h).

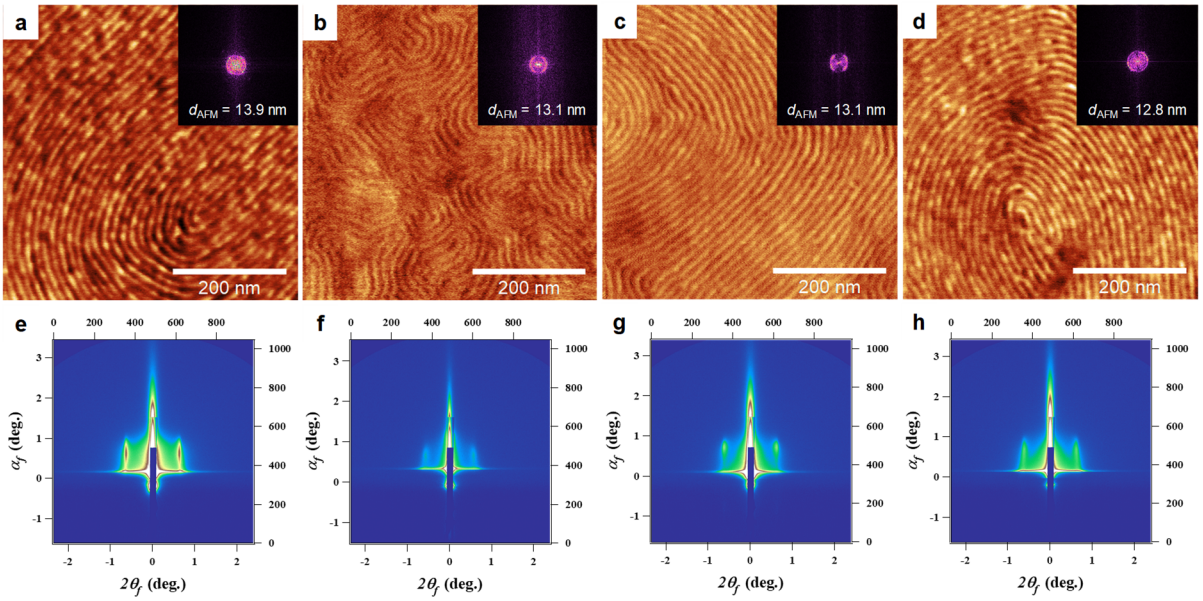

Figure 10. AFM phase images of the MH-*b*-PPO$_{4k}$-*b*-MH thin films prepared by μ-wave annealing in the presence of THF/H_2O (75:25, wt/wt) by varying the annealing time and temperature: (a) 100 °C for 2 s, (b) 100 °C for 5 s, (c) 100 °C for 10 s, and (d) 130 °C for 5 s. The insets in the AFM images show the corresponding FFT patterns, from which the d_{AFM} was estimated. (e), (f), (g), and (h) show their corresponding synchrotron GISAXS profiles. The thin films were prepared by spin coating a 2 wt% copolymer solution in ethanol+3 drops of DMF onto a silicon substrate.

Conclusion

In summary, we successfully synthesized high-χ AB- and ABA-type BCPs with different molecular weights and compositions based on commercially available poly(propylene glycol) and oligosaccharides, i.e. MH, MT, and Mal, using a click chemistry approach. The BCP systems self-assembled in the bulk state to provide longer-range-order HEX, BCC, and LAM nanostructures depending on their compositions and annealing temperatures with the *d* of 6.4–12.7 nm, as revealed by the SAXS analysis; this makes them excellent candidates for future nanopatterning applications. Most importantly, well-defined nanopatterns were also observed in the thermal and high-temperature solvent vapor-annealed thin films on the silicon wafers. The transition from the LAM to the HEX morphologies occurred when thin films were exposed to high-temperature solvent vapors using a μ-wave oven as the heating source. The preferential

swelling of the PPO block by the solvent vapors caused a change in the volume fraction of the BCPs, which should be responsible for this order-to-order transition. This transition of the parallel LAM morphology to the HEX morphology in the thin film state could be prevented using either nonselective solvents (e.g., methanol), which equally swell both the blocks during HTSVA, neutral interfaces during thermal annealing, or μ-wave heating without solvent vapors. These strategies are currently in progress in our laboratory. Finally, this work demonstrated that the carbohydrate-containing PPOs, i.e., "Sweet Pluronics", can advantageously replace the classical Pluronic systems (PEO-*b*-PPO and PEO-*b*-PPO-*b*-PEO) in different applications.

Acknowledgements

This work was financially supported by the JSPS Grant-in-Aid for Scientific Research (B) (No. 19H02769, T.S.; No. 20H02792, T.I.), JSPS Grant-in-Aid for Young Scientists (No. 18K14268, T.I.), Photo-excitonix Project (Hokkaido University, T.S.), Iketani Science and Technology Foundation (T.I.), Asahi Glass Foundation (T.I.), Toyota Riken (T.I.) and Polynat Carnot Institute (No. 16-CARN-025-01, R.B.). This work was partly performed under the approval of the Photon Factory Program Advisory Committee (Proposal No. 2017G589 and 2019G579). T.I. gratefully acknowledges the Nanotech CUPAL NRP program.

CRediT authorship contribution statement

Muhammad Mumtaz: Investigation, Methodology, Writing - Original Draft, Visualization. **Yasuko Takagi:** Investigation, Methodology, Visualization. **Hiroaki Mamiya:** Investigation. **Kenji Tajima:** Investigation, Supervision. **Cécile Bouilhace:** Investigation,

Methodology. **Takuya Isono:** Investigation, Methodology, Writing - Review & Editing, Visualization, Supervision, Funding acquisition. **Toshifumi Satoh:** Writing - Review & Editing, Supervision, Project administration, Funding acquisition. **Redouane Borsali:** Conceptualization, Writing - Review & Editing, Supervision, Project administration, Funding acquisition.

Declaration of Competing Interest

The authors declare that they have no known competing financial interests or personal relationships that could have appeared to influence the work reported in this paper.

Data availability

The raw/processed data required to reproduce these findings are available from the corresponding authors by request.

Appendix A. Supplementary material

Supplementary data to this article can be found online at https://doi.org/xxxxx.

References

(1) A. Nunns, J. Gwyther, I. Manners, Inorganic block copolymer lithography, Polymer 54 (2013) 1269−1284.

(2) T. Thurn-Albrecht, R. Steiner, J. DeRouchey, C. Stafford, M. E. Huang, M. Bal, M. Tuominen, C. J. Hawker, T. P. Russell, Nanoscopic templates from oriented block copolymer films, Adv. Mater. 12 (2000) 787–791.

(3) M. P. Stoykovich, P. F. Nealey, Block copolymers and conventional lithography, Mater. Today 9 (2006) 20–29.

(4) J. N. L. Albert, T. H. Epps, Self-assembly of block copolymer thin films, Mater. Today 13 (2010) 24–33.

(5) J. K. Kim, S. Y. Yang, Y. Lee, Y. Kim, Functional nanomaterials based on block copolymer self-assembly, Prog. Polym. Sci. 35 (2010) 1325–1349.

(6) M. A. Hillmyer, Nanoporous Materials from Block Copolymer Precursors, Adv. Polym. Sci. 190 (2005) 137–181.

(7) D. Bratton, D. Yang, J. Y. Dai, C. K. Ober, Recent progress in high resolution lithography, Polym. Adv. Technol. 17 (2006) 94–103.

(8) H. H. Solak, C. David, J. Gobrecht, V. Golovkina, F. Cerrina, S. O. Kim, P. F. Nealey, Sub-50 nm period patterns with EUV interference lithography, Microelectron. Eng. 67 (2003) 56–62.

(9) R. H. Stulen, D. W. Sweeney, Extreme ultraviolet lithography, IEEE J. Quantum Electron. 35 (1999) 694–699.

(10) C. Wagner, N. Harned, Lithography gets extreme, Nat. Photonics 4 (2010) 24–26.

(11) J. Benschop, V. Banine, S. Lok, E. Loopstra, Extreme ultraviolet lithography: Status and prospects, J. Vac. Sci. Technol., B 26 (2008) 2204–2207.

(12) M. Park, C. Harrison, P. M. Chaikin, R. A. Register, D. H. Adamson, Block copolymer lithography: periodic arrays of ~10^{11} holes in 1 square centimeter, Science 276 (1997) 1401–1404.

(13) R. R. Li, P. D. Dapkus, M. E. Thompson, W. G. Jeong, Dense arrays of ordered GaAs nanostructures by selective area growth on substrates patterned by block copolymer lithography, Appl. Phys. Lett. 76 (2000) 1689–1691.

(14) T. Thurn-Albrecht, J. Schotter, G. A. Kästle, N. Emley, T. Shibauchi, L. Krusin-Elbaum, K. Guarini, C. T. Black, M. T. Tuominen, T. P. Russell, Ultrahigh-density nanowire arrays grown in self-assembled diblock copolymer templates, Science 290 (2000) 2126–2129.

(15) H. C. Kim, X. Q. Jia, C. M. Stafford, D. H. Kim, T. J. McCarthy, M. Tuominen, C. J. Hawker, T. P. Russell, A Route to Nanoscopic SiO_2 Posts via Block Copolymer Templates. Adv. Mater. 13 (2001) 795–797.

(16) W. A. Lopes, H. M. Jaeger, Hierarchical self-assembly of metal nanostructures on diblock copolymer scaffolds, Nature 414 (2001) 735–738.

(17) J. Y. Cheng, C. A. Ross, V. Z.-H. Chan, E. L. Thomas, R. G. H. Lammertink, G. J. Vancso, Formation of a cobalt magnetic dot array via block copolymer lithography, Adv. Mater. 13 (2001) 1174–1178.

(18) J. Y. Cheng, A. M. Mayes, C. A. Ross, Nanostructure engineering by templated self-assembly of block copolymers, Nat. Mater. 3 (2004) 823–828.

(19) R. Ruiz, H. M. Kang, F. A. Detcheverry, E. Dobisz, D. S. Kercher, T. R. Albrecht, J. J. de Pablo, P. F. Nealey, Density Multiplication and Improved Lithography by Directed Block Copolymer Assembly, Science 321 (2008) 936–939.

(20) J. Y. Cheng, C. A. Ross, H. I. Smith, E. L. Thomas, Templated Self-Assembly of Block Copolymers: Top-Down Helps Bottom-Up, Adv. Mater. 18 (2006) 2505–2521.

(21) S. O. Kim, H. H. Solak, M. P. Stoykovich, N. J. Ferrier, J. J. de Pablo, P. F. Nealey, Epitaxial self-assembly of block copolymers on lithographically defined nanopatterned substrates, Nature 424 (2003) 411–414.

(22) M. W. Matsen, F. S. Bates, Unifying Weak- and Strong-Segregation Block Copolymer Theories, Macromolecules, 29 (1996) 1091–1098.

(23) L. Leibler, Theory of Microphase Separation in Block Copolymers, Macromolecules 13 (1980) 1602–1617.

(24) F. S. Bates, G. H. Fredrickson, Block Copolymer Thermodynamics: Theory and Experiment, Annu. Rev. Phys. Chem. 41 (1990) 525–557.

(25) C. Sinturel, F. S. Bates, M. A. Hillmyer, High χ–Low N Block Polymers: How Far Can We Go?, ACS Macro Lett. 4 (2015) 1044–1050.

(26) W. J. Durand, G. Blachut, M. J. Maher, S. Sirard, S. Tein, M. C. Carlson, Y. Asano, S. X. Zhou, A. P. Lane, C. M. Bates, Design of high-χ block copolymers for lithography, J. Polym. Sci. Part A: Polym. Chem. 53 (2015) 344−352.

(27) K. Yoshida, L. Tian, K. Miyagi, A. Yamazaki, H. Mamiya, T. Yamamoto, K. Tajima, T. Isono, T. Satoh, Facile and Efficient Modification of Polystyrene-*block*-poly(methyl methacrylate) for Achieving Sub-10 nm Feature Size, Macromolecules 51 (2018) 8064−8072.

(28) T. Sesimo, R. Maeda, R. Odashima, Y. Takenaka, D. Kawana, K. Ohmori, T. Hayakawa, Perpendicularly oriented sub10-nm block copolymer lamellae by atmospheric thermal annealing for one minute, Sci. Rep. 6 (2016) 19481.

(29) J. M. Kim, Y. H. Hur, J. W. Jeong, T. W. Nam, J. H. Lee, K. Jeon, Y. Kim, Y. S. Jung, Block Copolymer with an Extremely High Block-to-Block Interaction for a Significant Reduction of Line-Edge Fluctuations in Self-Assembled Patterns, Chem. Mater. 28 (2016) 5680−5688.

(30) W. Zhang, M. Huang, S. al Abdullatif, M. Chen, Y. Shao-Horn, J. A. Johnson, Reduction of (Meth)acrylate-Based Block Copolymers Provides Access to Self-Assembled Materials with Ultrasmall Domains, Macromolecules 51 (2018) 6757−6763.

(31) J. G. Kennemur, L. Yao, F. S. Bates, Hillmyer, M. A. Sub-5 nm Domains in Ordered Poly(cyclohexylethylene)-*block*-poly(methyl methacrylate) Block Polymers for Lithography, Macromolecules 47 (2014) 1411–1418.

(32) Y. Luo, D. Montarnal, S. Kim, W. Shi, K. Barteau, C. W. Pester, P. D. Hustad, M. D. Christianson, G. H. Fredrickson, E. J. Kramer, C. J. Hawker, Poly(dimethylsiloxane-*b*-methyl methacrylate): A Promising Candidate for Sub-10 nm Patterning, Macromolecules 48 (2015) 3422–3430.

(33) S. Jo, S. Jeon, T. Jun, C. Park, D. Y. Ryu, Fluorine-Containing Styrenic Block Copolymers toward High χ and Perpendicular Lamellae in Thin Films, Macromolecules 51 (2018) 7152−7159.

(34) K. Azuma, J. Sun, Y. Choo, Y. Rokhlenko, J. H. Dwyer, B. Schweitzer, T. Hayakawa, C. O. Osuji, P. Gopalan, Self-Assembly of an Ultrahigh-χ Block Copolymer with Versatile Etch Selectivity, Macromolecules 51 (2018) 6460–6467.

(35) K. Aissou, M. Mumtaz, G. Fleury, G. Portale, C. Navarro, E. Cloutet, C. Brochon, C. A. Ross, G. Hadziioannou, Sub-10 nm Features Obtained from Directed Self-assembly of Semicrystalline Block Copolymer Thin Films, Advanced Materials 27 (2015) 261–265.

(36) J. D. Cushen, I. Otsuka, C. M. Bates, S. Halila, S. Fort, C. Rochas, J. A. Easley, E. L. Rausch, A. Thio, R. Borsali, C. G. Willson, C. J. Ellison, Oligosaccharide/Silicon-Containing Block Copolymers with 5 nm Features for Lithographic Applications, ACS Nano 6 (2012) 3424−3433.

(37) T. Isono, I. Otsuka, Y. Kondo, S. Halila, S. Fort, C. Rochas, T. Satoh, R. Borsali, T. Kakuchi, Sub-10 nm Nano-Organization in AB_2- and AB_3-Type Miktoarm Star Copolymers Consisting of Maltoheptaose and Polycaprolactone, Macromolecules 46 (2013) 1461−1469.

(38) T. Isono, N. Kawakami, K. Watanabe, K. Yoshida, I. Otsuka, H. Mamiya, H. Ito, T. Yamamoto, K. Tajima, R. Borsali, T. Satoh, Microphase separation of carbohydrate-based star-block copolymers with sub-10 nm periodicity, Polym. Chem. 10 (2019) 1119−1129.

(39) I. Otsuka, S. Tallegas, Y. Sakai, C. Rochas, S. Halila, S. Fort, A. Bsiesy, T. Baron, R. Borsali, Control of 10 nm scale cylinder orientation in self-organized sugar-based block copolymer thin films, Nanoscale 5 (2013) 2637−2641.

(40) T. Isono, B. J. Ree, K. Tajima, R. Borsali, T. Satoh, Highly Ordered Cylinder Morphologies with 10 nm Scale Periodicity in Biomass-Based Block Copolymers, Macromolecules 51 (2018) 428–437.

(41) L. Barreda, Z. Shen, Q. P. Chen, T. P. Lodge, J. I. Siepmann, M. A. Hillmyer, Synthesis, Simulation, and Self-Assembly of a Model Amphiphile To Push the Limits of Block Polymer Nanopatterning, Nano Lett. 19 (2019) 4458−4462.

(42) S. R. Nowak, W. Hwang, L. R. Sita, Dynamic Sub-10-nm Nanostructured Ultrathin Films of Sugar–Polyolefin Conjugates Thermoresponsive at Physiological Temperatures, J. Am. Chem. Soc. 139 (2017) 5281−5284.

(43) Y. Liao, W.-C. Chen, R. Borsali, Carbohydrate-Based Block Copolymer Thin Films: Ultrafast Nano-Organization with 7 nm Resolution Using Microwave Energy, Adv. Mater. 29 (2017) 1701645.

(44) Y. Liao, K. Liu, W.-C. Chen, B. Wei, R. Borsali, Robust Sub-10 nm Pattern of Standing Sugar Cylinders via Rapid “Microwave Cooking”, Macromolecules 52 (2019) 8751–8758.

(45) I. R. Schmolka, A Review of Block Copolymer Surfactants, J. Am. Oil Chem. Soc. 54 (1977) 110-116.

(46) H. F. Mark, N. M. Bikales, C. G. Overberger, G. Menges, J. I. Kroschwitz (Eds.), Encyclopedia of Polymer Science and Engineering, John Wiley & Sons, Inc.: New York, 1985.

(47) S. Gupta, R. Tyagi, V. S. Parmar, S. K. Sharma, R. Haag, Polyether based amphiphiles for delivery of active components, Prog. Polym. Sci. 53 (2012) 3053−3078.

(48) Y. Nabae, S. Nagata, K. Ohnishi, Y. Liu, L. Sheng, X. Wang, T. Hayakawa, Block copolymer templated carbonization of nitrogen containing polymer to create fine and mesoporous carbon for oxygen reduction catalyst, J. Polym. Sci. Part A: Polym. Chem. 55 (2017) 464–470.

(49) D. Hermida-Merino, G. E. Newby, I. W. Hamley, W. Hayes, A. Slark, Microphase separation induced in the melt of Pluronic copolymers by blending with a hydrogen bonding urea–urethane end-capped supramolecular polymer, Soft Mater 11 (2015) 5799−5803.

(50) V. K. Daga, J. J. Watkins, Hydrogen-Bond-Mediated Phase Behavior of Complexes of Small Molecule Additives with Poly(ethylene oxide-*b*-propylene oxide-*b*-ethylene oxide) Triblock Copolymer Surfactants, Macromolecules 43 (2010) 9990−9997.

(51) T. Nishimura, Y. Sasaki, K. Akiyoshi, Biotransporting Self-Assembled Nanofactories Using Polymer Vesicles with Molecular Permeability for Enzyme Prodrug Cancer Therapy, Adv. Mater. 29 (2017) 1702406.

(52) A. K. Khandpur, S. Foerster, F. S. Bates, I. W. Hamley, A. J. Ryan, W. Bras, K. Almdal, K. Mortensen, Polyisoprene-polystyrene Diblock Copolymer Phase Diagram near the Order-disorder Transition, Macromolecules 28 (1995) 8796−8806.

(53) S. Sakurai, T. Hashimoto, L. J. Fetters, Thermoreversible Cylinder−Sphere Transition of Polystyrene-*block*-polyisoprene Diblock Copolymers in Dioctyl Phthalate Solutions, Macromolecules 29 (1996) 740−747.

(54) M. F. Schulz, F. S. Bates, K. Almdal, K. Mortensen, Epitaxial Relationship for Hexagonal-to-Cubic Phase Transition in a Block Copolymer Mixture, Phys. Rev. Lett. 73 (1994) 86–89.

(55) S. Shirke, R. D. Ludescher, Molecular mobility and the glass transition in amorphous glucose, maltose, and maltotriose, Carbohydr. Res. 340 (2005) 2654–2660.

(56) K. Imamura, K. Sakaura, K.-i. Ohyama, A. Fukushima, H. Imanaka, T. Sakiyama, K. Nakanishi, Temperature Scanning FTIR Analysis of Hydrogen Bonding States of Various Saccharides in Amorphous Matrixes below and above Their Glass Transition Temperatures, *J. Phys. Chem. B* 110 (2006) 15094–15099.